NANO · MICRO small
www.small-journal.com

Conductive Polymer-Coated 3D Printed Microneedles: Biocompatible Platforms for Minimally Invasive Biosensing Interfaces

*Antonios Keirouz, Yasemin L. Mustafa, Joseph G. Turner, Emily Lay, Ute Jungwirth, Frank Marken, and Hannah S. Leese**

Conductive polymeric microneedle (MN) arrays as biointerface materials show promise for the minimally invasive monitoring of analytes in biodevices and wearables. There is increasing interest in microneedles as electrodes for biosensing, but efforts have been limited to metallic substrates, which lack biological stability and are associated with high manufacturing costs and laborious fabrication methods, which create translational barriers. In this work, additive manufacturing, which provides the user with design flexibility and upscale manufacturing, is employed to fabricate acrylic-based microneedle devices. These microneedle devices are used as platforms to produce intrinsically-conductive, polymer-based surfaces based on polypyrrole (PPy) and poly(3,4-ethylenedioxythiophene)-poly(styrenesulfonate) (PEDOT:PSS). These entirely polymer-based solid microneedle arrays act as dry conductive electrodes while omitting the requirement of a metallic seed layer. Two distinct coating methods of 3D-printed solid microneedles, in situ polymerization and drop casting, enable conductive functionality. The microneedle arrays penetrate ex vivo porcine skin grafts without compromising conductivity or microneedle morphology and demonstrate coating durability over multiple penetration cycles. The non-cytotoxic nature of the conductive microneedles is evaluated using human fibroblast cells. The proposed fabrication strategy offers a compelling approach to manufacturing polymer-based conductive microneedle surfaces that can be further exploited as platforms for biosensing.

1. Introduction

Point-of-care (POC) technologies tend to rely on exploring non- or minimally invasive routes in a bid to acquire physiological information for diagnostic or disease monitoring purposes, preferably those attainable at the intervention site and time of care.[1] When considering differing types of diagnostic tools for POC healthcare monitoring, on-patch biosensors have emerged as a compelling technology in transitioning from invasive to minimally invasive personalized healthcare and precision medicine.[2] Biosensor advancements thus far have relied on breakthroughs in miniaturization and customization of electronic elements to improve functionality.[3]

Microneedle (MN) array technologies have captured attention as potential POC devices, due to their capabilities to act as multifunctional platforms for pain-free transdermal extraction of analytes and drug delivery.[4,5] Microneedles present an attractive approach to developing wearable biosensors capable of multiplexing and continuous monitoring of clinically

A. Keirouz, Y. L. Mustafa, J. G. Turner, H. S. Leese
Materials for Health Lab
Department of Chemical Engineering
University of Bath
Bath BA2 7AY, UK
E-mail: h.s.leese@bath.ac.uk

The ORCID identification number(s) for the author(s) of this article can be found under https://doi.org/10.1002/smll.202206301.

DOI: 10.1002/smll.202206301

A. Keirouz, Y. L. Mustafa, J. G. Turner, H. S. Leese
Centre for Biosensors
Bioelectronics and Biodevices (C3Bio)
University of Bath
Bath BA2 7AY, UK

E. Lay, U. Jungwirth
Department of Life Sciences
University of Bath
Bath BA2 7AY, UK

E. Lay, U. Jungwirth
Centre for Therapeutic Innovation
University of Bath
Bath BA2 7AY, UK

F. Marken
Department of Chemistry
University of Bath
Claverton Down, Bath BA2 7AY, UK

relevant targets present in the interstitial fluid.[6] Conventionally, solid microneedles are produced via microfabrication techniques such as etching, laser ablation, micromilling, photolithography, plasma-enhanced chemical vapor deposition, and micro-molding, often designed with the utilization of materials including silicon, glass, ceramic, metals, hydrogels, and polymers.[7–9] Although these methods obtain fine and reproducible microneedles, they have high manufacturing costs, complicated labor-intensive fabrication procedures that lack automation, and can limit the manufacture of microneedles on a larger economic scale. Advancements in additive manufacturing can address these limitations by introducing a scalable and cost-effective route for microneedle design and development.[7]

At present, the implementation of microneedle arrays as interface materials for electrochemical sensing has predominately relied on metallic microneedles (e.g., stainless steel), or metalized coatings consisting of thin metal films (predominately gold and platinum), required to obtain the conductive layer for signal transduction.[10] Although incorporating such materials remain the gold standard due to their well-understood properties, such as chemical stability and electrical consistency, they also lack mechanical flexibility, ease of processibility, and often present poor biocompatibility, in conjunction with loss of functionality over time.[11]

Intrinsically conducting polymers such as PPy and PEDOT:PSS can prove impressive alternatives for the development of conductive microneedle surfaces due to their excellent electrical properties even under mechanical stress.[12,13] Further, the noncytotoxic nature and good biocompatibility of these conducting polymers have been readily demonstrated via in vivo and in vitro studies.[14–18]

Conducting polymers can be introduced on the surface of micro-/nanostructured materials via processes such as chemical or electrochemical deposition and solution casting.[19] Electroresponsive materials such as PPy and PEDOT:PSS have been widely employed as interfacial materials for the detection of, among others, small molecules,[20] DNA,[21] viruses,[22] and cell function.[23] Thus, these conducting polymers have been extensively examined and adopted within the biomedical domain.[24] Such characteristics have been attributed to the conjugated π orbitals within the polymeric backbone of PPy[25] and the positively charged conjugated PEDOT and negatively charged saturated PSS within the organic structural framework of PEDOT:PSS.[26]

Although intrinsically conducting polymers (ICPs) can, to an extent, mimic the electrical behavior of metallic conductivity or act as semiconductors – while being more easily processable,[24] challenges associated with achieving reproducible homogenous coatings that retain the microneedles' micromorphology must be considered.[27] Microneedle skin insertion can be evaluated via the utilization of an ex vivo skin model and provides an excellent mimic of human skin, owing to similarities in epidermis thickness and number of cell layers to that of human skin.[28] Thus, for the purposes of this study, an ex vivo porcine model has been implemented to assess microneedle penetration capabilities.

This work has designed a platform technology of entirely polymer-based conductive microneedle arrays which have the potential to facilitate developments toward bioinspired and smart medical devices. By advancing our available toolkits for designing conductive microneedle systems via additive manufacturing and further enhancing these by the incorporation of PPy and PEDOT:PSS, these platforms have the potential to drive disease diagnostics and drug delivery methods to an efficiency that outperforms current practices.

The significant technological progress in developing arrays for biosensing applications has been coupled with the need for alternative, reproducible, and scalable methodologies that produce stable conductive microneedle surfaces. We answer this need through the development of polymeric-conductive-microneedle arrays via two new approaches: we introduce a 360°-conductive polymeric coating onto the surface of stereolithography 3D printing solid microneedles via (1) in situ oxidative chemical polymerization of pyrrole and (2) casting of PEDOT:PSS in order to assess the ability for these conductive polymer microneedle arrays to perform as biocompatible platforms for minimally invasive biosensing interfaces.

2. Results and Discussion

In the present study, solid microneedle patches consisting of 45 conically-shaped needles (600 µm in height) arranged atop a 10 mm disc (500 µm in thickness) were produced via stereolithography 3D printing using a computer-aided design (CAD) (Figure S1(i), Supporting Information). The implementation of CAD and 3D printing enables facile structural and configurational modifications, providing flexibility in the microneedle design and tailor-made microneedle dimensions, structure, architecture, and in-principle, composition. Such adaptability can incite the development of application-specific microneedle devices. Opting to use 3D printing for microneedle development can provide a scalable, consistently reproducible, and significantly cheaper manufacturing approach.[29,30] In our work, manufacturing 182 microneedle array devices takes ≈ 5 h at high resolution (25 µm), consuming ≈ 20 mL of the methacrylic acid-based resin, while costing 4 USD or, i.e., 2 cents per microneedle device platform (Figure S1(ii), Supporting Information).

A 360° electroactive layer of PPy or PEDOT:PSS was deposited onto the 3D-printed microneedles via two distinct methodological approaches (**Figure 1**(i)). Deposited layers of PEDOT:PSS were achieved by casting a predetermined volume (25 µL) of the polymer onto both sides of the microneedles, subsequent to surface activation of the microneedle array via oxygen plasma treatment (Figure 1(i-a)). PPy deposition was attained via in situ oxidative chemical polymerization of pyrrole in the presence of ferric chloride as the oxidizing agent (Figure 1(i-b) and Figure S2, Supporting Information). Unlike traditional electropolymerization methods, wherein the conducting polymer is formed onto a conducting substrate, this chemical approach encourages rapid mass production of conducting polymers onto the surface of a solid non-conductive material.

As demonstrated by recent literature within the field of microneedles, there is heavy reliance upon the presence of a metallic seed layer to produce conductive microneedle surfaces.[31,32] However, here, for the first time, we report the fabrication of uniformly conductive microneedle devices, entirely produced from polymers, bypassing the *sine qua* non-requirement of a metallic seed layer for the deposition of a

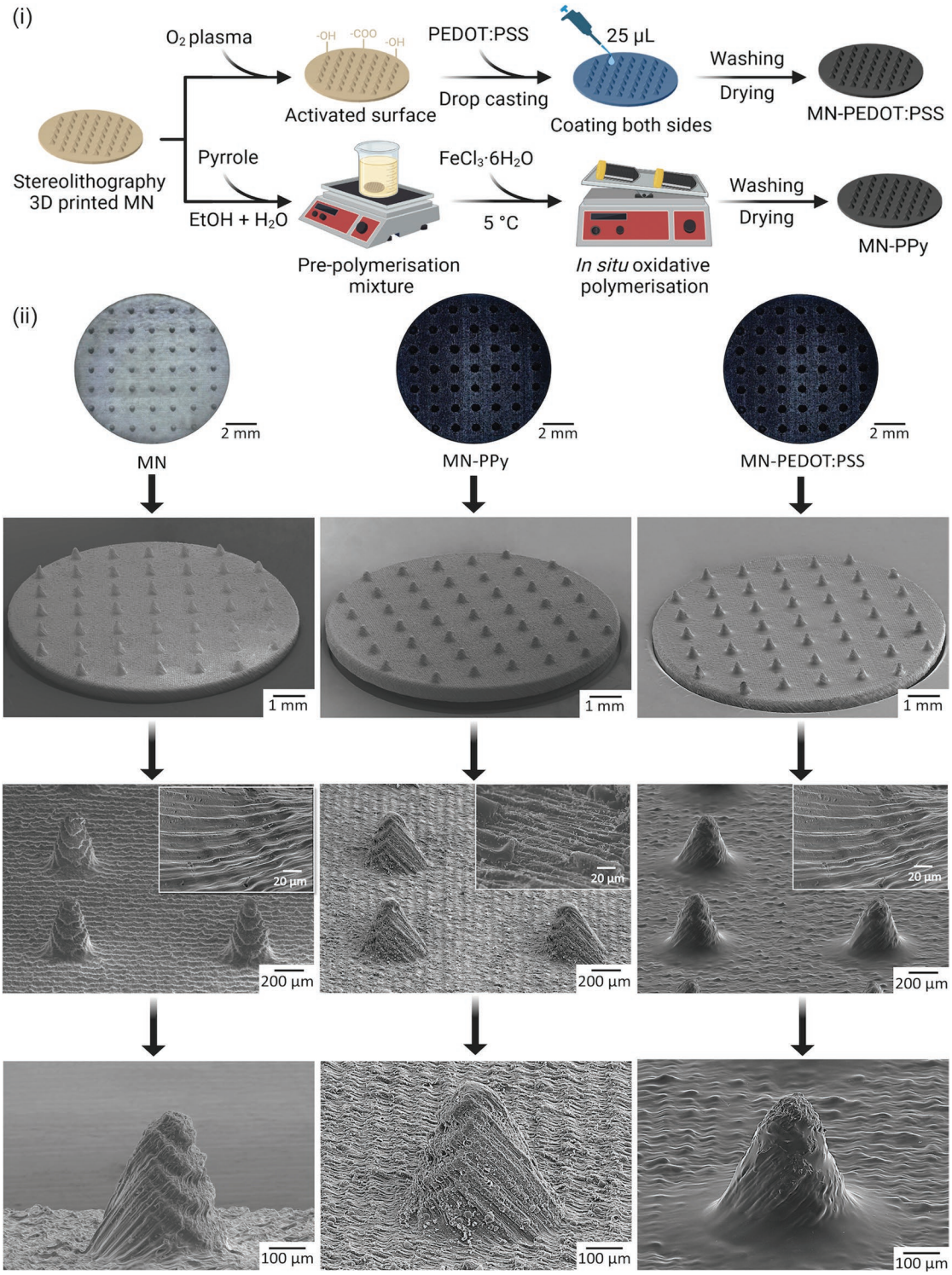

Figure 1. 3D printed microneedle (MN) arrays adapted to produce polymeric conductive surfaces. (i) Schematic representation of the two distinct approaches implemented for coating a) PEDOT:PSS and b) the in situ synthesis of PPy. (ii) Macroscopic images and SEM micrographs of the uncoated, PPy, and PEDOT:PSS-coated microneedle surfaces.

conductive polymer layer, thus generating polymer composite conductive microneedle patches in a straightforward two-step process (Figure 1(i)).

Following successive washings and thorough drying, the microneedle-PPy (MN-PPy) and microneedle-PEDOT:PSS-coated (MN-PEDOT:PSS) composites were morphologically

assessed, revealing the architectural framework of the uncoated and coated devices (Figure 1(ii)). The macroscopic images highlight the uniform morphology of the MN-PPy and MN-PEDOT:PSS-coated samples, reinforced by their structural resemblance to that of uncoated microneedles. Further details provided by the SEM micrographs emphasize the homogenous microstructural characteristics of the coated microneedles, where the addition of polymer coating layers appear to decrease the surface roughness of the pristine microneedles (Figure 1(ii)). Furthermore, the PEDOT:PSS coating shows reduced needle surface roughness, suggestive of a marginally thicker coating, as the morphology of the base structure in all microneedle samples appears relatively similar. The smoothness was further validated by assessing the surface roughness of the pristine 3D-printed microneedles and coated surfaces via atomic force microscopy. As depicted in Figure S3 (Supporting Information), there is a notable decrease in surface roughness between the uncoated microneedle group (450 ± 50.3 nm) and the MN-PPy (274 ± 285 nm) and substantially smoother MN-PEDOT:PSS (44 ± 28.6 nm) groups. Surface roughness can be an indicator of the microneedle structural composition, providing important information about the selected manufacturing approach. Surface roughness can also be an important measure of coating homogeneity and influence the hydrophilicity of the coated surfaces. Thus, it can be ascertained that via the described methods of conductive polymer deposition, it is possible to attain smooth homogenous coatings on these miniaturized devices (Figure S4, Supporting Information).

To further validate the versatility of the designed conductive microneedle fabrication protocol, an alternative material was employed to form the base microneedle array. Instead, the methacrylic acid-based resin was replaced with bisphenol A diglycidyl ether (BADGE) resin, a renowned biocompatible resin.[33,34] To support the versatility of the process, PEDOT:PSS was used to coat the microneedles using the same methodology, as shown in Figure 1(i-a). All information regarding the synthesis of conductive BADGE microneedle devices and associated characterizations can be found in the Supplementary Information.

As an important first-line analytical tool, FTIR was used to identify the chemical composition of the two coatings; including the successful synthesis of PPy and the homogenous dispersion of PEDOT:PPS onto the microneedles. The FTIR spectra of the microneedle devices are presented in **Figure 2**(i), the spectra of the raw materials can be found in Figure S5 (Supporting Information).

The MN-PPy FTIR spectrum (Figure 2(i-a)) agrees with previously reported literature.[35–38] The heterocyclic aromatic ring is defined by the C-C stretching vibrations at 1444 and 1280 cm^{-1}, the C=C stretching vibration at 1529 cm^{-1}, the N−C stretching vibration at 1680 cm^{-1}, and at 1280 cm^{-1} the in-plane deformation of the secondary amine group bound onto the pyrrole ring. The absorption at 1021, 1150, and 1377 cm^{-1} can be ascribed to C−H/N−H in-plane deformation modes (pyrrole ring breathing vibrations).[39,40] The peaks at the lower spectrum, at 960 and 870 cm^{-1}, can be attributed to the out-of-plane C−C/C−H deformation vibrations of the pyrrole units, which are indicative of pyrrole polymerization.[41,42]

The MN-PEDOT:PSS (Figure 2(i-b)) presents PEDOT's major peak at 1460 cm^{-1} attributed to C=C stretching of the thiophene ring, at 1268 cm^{-1} due to the symmetric C−C stretching of the thiophene inter-ring, at 1150 cm^{-1} due to the C−O−C stretching, and at 1070 cm^{-1} it is assignable to the C−C−O stretching of the ethylenedioxy groups.[43–45] In addition, the absorptions at 953, 870, and 711 cm^{-1} can be attributed to the C−S−C of the thiophene ring backbone.[46] The PSS presents symmetric and asymmetric O=S=O stretches at 1380 and 1150 cm^{-1}, respectively,[47] wherein the peak at 1070 cm^{-1} can be attributed to an S−O stretch due to the S-phenyl bond of the sulfonate.[43–45] In addition, the absorptions at 953, 870, and 711 cm^{-1} can be attributed to the C−S−C of the thiophene ring backbone.[46] The PSS presents symmetric and asymmetric O=S=O stretches at 1380 and 1150 cm^{-1}, respectively,[47] wherein the peak at 1070 cm^{-1} can be attributed to an S−O stretch due to the S-phenyl bond of the sulfonate.[45] The FTIR spectrum of BADGE-PEDOT:PSS microneedles can be observed in Figure S6 (Supporting Information).

Although the chemical composition of the photocurable high-temperature resin used to produce the microneedle arrays is not made commercially available by the manufacturer, the FTIR spectrum Figure 2(i-c) shares several characteristic absorption peaks associated with proprietary methacrylate compounds, such as polymethylmethacrylate (PMMA).[48] The characteristic absorption bands at 1720 and 1695 cm^{-1} can be attributed to the C=O stretching of the carbonyl groups.[49] The acrylate's C=C stretch and C−H twist (or the wag of $-CH_2$) can be found at 1383 and 1456 cm^{-1}, respectively.[50] The two bands at 1250 and 1154 cm^{-1} can be assigned to the C−O stretch and antisymmetric C−C−O stretching, respectively.[51] The peaks at 750, 810, and 955 cm^{-1} can be associated with C−H wagging (skeletal mode), C−O−C symmetric stretching, and CH_3 rocking vibration of the ester groups, respectively.[51]

The three spectra present similar vibrational features in the higher wavenumber region (4000–2000 cm^{-1}), with the peak at 2979 cm^{-1} corresponding to asymmetric and symmetric CH_2 vibration (stretch) at relatively similar intensities, whereas the stretching at the 3350–3300 cm^{-1} regions can be assigned to the presence of -OH. Within this region, there are also subtle differences in band positions, widths, and relative intensities at lower frequencies (2000–500 cm^{-1}), indicative of different hybridizations distinctive to each coating. The absorption band at 2360 cm^{-1} can be attributed to atmospheric CO_2.

Raman spectroscopy further demonstrates the presence of each conductive polymer's corresponding functional groups in contrast to the pristine microneedle trace (Figure 2(ii-c)). Characteristic peaks attributed to the S−S, S−C, C_4H_4S, and R_SO_2OH bonds signify the presence of disulfide, organosulfur, aromatic ring, and sulfonic acid functional groups existing within the structure of PEDOT:PSS, while observable C-H and C_6H_3N bonds strongly suggest the presence of aromatic and alkane functional groups available in the structure of PPy.[52] The highlighted functional features provide structural evidence inferring the successful preparation of MN-PEDOT:PSS and MN-PPy structures (see Table S1, Supporting Information for further data). Visible O-H, C=O, and CH_2 bonds representative of carboxylic acid, and alkane functional groups present in the structure of the predominantly methacrylic-based microneedles

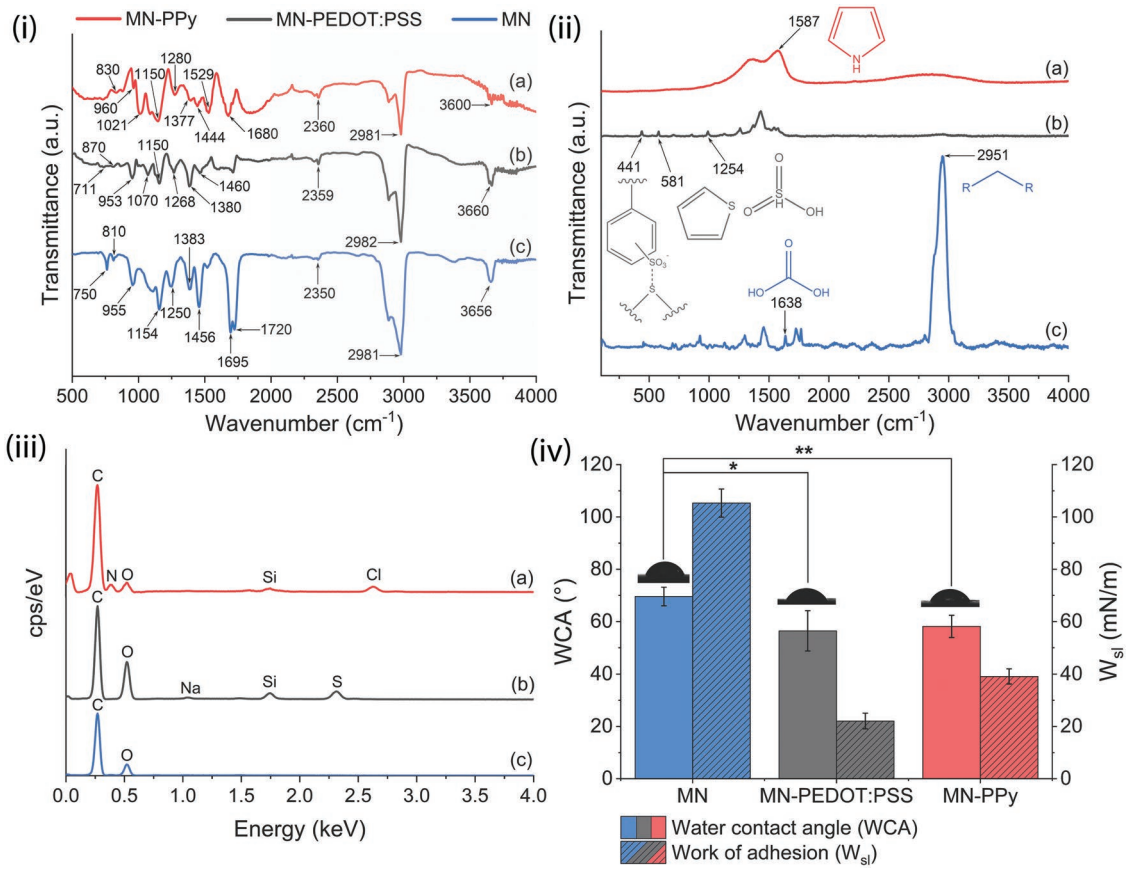

Figure 2. Chemical analysis, representative (i) ATR-FTIR and (ii) Raman spectra of the a) MN-PPy, b) MN-PEDOT:PSS and uncoated c) MN surfaces. (iii) Representative EDX elemental mapping graphs. (iv) Impact of the polymeric coatings pertinent to the surface properties of the microneedles. Static water contact angle and liquid-solid work adhesion measurements of flat-coated and uncoated surfaces, with representative images. Data are shown as mean ± SD, $n = 6$. Significant differences for each group (Student's t-test): $^{*}p \leq 0.05$, $^{**}p \leq 0.01$.

are present.[52] Distinguishing features of the microneedle trace are not evident in the traces of MN-PEDOT:PSS and MN-PPy (Figure 2(ii-a,b,c)), with the exception of the modest peak ~ 2950 cm^{-1}, indicative of the alkane functional group, due to the conductive polymer coatings shrouding the pristine microneedle signal, which corroborates the effective coating methods of each microneedle structure. The Raman spectra of the pristine materials can be found in Figure S7 (Supporting Information) and information relating to BADGE-PEDOT:PSS MNs is visible in Figure S8 (Supporting Information).

Energy dispersive X-ray spectroscopy (EDX) elemental maps (Figure 2(iii)) designate C, O peaks to pristine microneedles; C, O, N, Cl peaks to MN-PPy; and C, O, S peaks to the MN-PEDOT:PSS group. Table S2 (Supporting Information) summarises the quantitative contents and theoretical values of the constituent compounds. The elemental atomic percentages are in agreement with the theoretical amounts enumerated for each compound, reaffirming the presence of the PEDOT:PSS coating and the successful synthesis of PPy onto the microneedle surface. Populations of N (exp. atom. 22.34 ± 0.40%, theoretical atom. 20%), Cl (exp. atom. 4.60 ± 0.08%), and S (exp. atom. 8.71 ± 0.28%, theoretical atom. 9.52%) are indicative of PPy and PEDOT:PSS, respectively. The presence of small amounts of Cl anions is indicative of the PPy synthesis route via ferric chloride, whereas the absence of Fe is due to the rigorous washing methodology followed. The high atomic percentage of O (31.94 ± 0.04%) in the pristine microneedle is also present in significantly smaller amounts in the MN-PPy specimens (9.94 ± 0.44%). For MN-PEDOT:PSS, small amounts of Na (3.68 ± 0.17%) could be attributed to residual sodium ions present in the aqueous dispersion and the washes in phosphate-buffered saline.

Changes in the wettability properties were quantitatively assessed through water contact angle (WCA) measurements taken under ambient conditions. The pristine uncoated microneedle surface exhibited a moderately hydrophilic 69.6° ± 3.6° WCA (Figure 2(iv)). The adhesion energy between a solid and liquid surface increases by increasing the hydrophilicity of the solid surface.[53] In both instances, the surface state of the MN-PPy and MN-PEDOT:PSS coatings significantly improved the moderately hydrophilic nature of the pristine polymer microneedles, reducing the WCA to 58.1° ± 4.3° and 56.3° ± 7.7°, respectively.

The static WCA of PPy-coated flat surfaces has been previously reported to be between 20° and 75°, depending on the coating's microstructure, roughness, and PPy synthesis protocol.[39,40] In this work, the PPy coating positively influenced the hydrophilic properties of the pristine polymer microneedle surface, further

lowering its WCA. PEDOT:PSS has a broad WCA reported in the literature, ranging from 10° to 90°, depending upon the dispersion solvent (such as water or ethanol), the hydration state, the coating method, and the technique chosen to obtain the measurements.[41,42] Further, the significant difference in the hydrophobicity between PEDOT and PSS means that even small changes in the relative amount of these two molecules could have an impact on the material's wettability.[54] In both instances, the addition of the conductive layer onto the microneedles significantly improves the wetting behavior of the material in water.[41,42]

In the case of the pristine microneedles, our reported value is lower than in previously reported work using the same resin that determined the WCA to be 97.0° ± 6.7°.[55] Similar to our work, the sessile droplet method was used to measure the contact angle of a deionized water droplet 30 s after settling on the surface, but the 3D printed constructs were subject to post-curing for 30 min at 60 °C (in contrast to 2 h at 80 °C in our work), and the surfaces were also subsequently polished using grit sandpaper. Irrespective of the polishing step, the reported micrographs depict a rougher surface than the one attained in our work. Tzivelekis et al.,[56] using the same printing resin, reported a WCA of 80° after curing the specimens under a 355 nm, 80 W cm^{-2} source for 1 h. In our work, as depicted in the previously described SEM micrographs (Figure 1(ii)), the pristine microneedles were printed at a 45° angle to increase the printing resolution further by reducing the touchpoint size and attaining a finer needle micromorphology; however, this has also made the surface deposition rougher, possibly affecting the water droplet settlement. This variability demonstrates that differences in roughness or residual differences due to curing time can significantly affect photopolymer wetting behavior. Further, it has been shown that variations in hardening/solidification methods can lead to structural defects such as residual stresses, warping, and voids, which in turn can affect the material wettability properties.[57] Overall, in this work, we report that the addition of the conductive polymer coatings onto the surface of the 3D printed microneedles has reduced the WCA of the pristine material through the hydrophilic nature of the polymers chosen and the formation of a smoother coated surface.

To characterize the mechanical strength of the pristine and coated microneedle arrays, a compressive force of up to 4 N was applied. The resultant displacement was recorded (**Figure 3**(i)), and the subsequent stress-strain curves calculated (Figure 3(ii)). The total contact area between the microneedle tips and upper titanium plate was ≈ 0.09 mm^2. A force of 0.08 N·$Needle^{-1}$ is widely reported to be the minimum force required for successful skin penetration,[58] with more recent research reporting the minimum force required to pierce skin to be as little as 0.045 N·$Needle^{-1}$.[59] Taking the higher end of the reported literature, a minimum total force of 3.6 N is required for this microneedle design to penetrate skin. Subject to mechanical compression, all microneedles showed no demonstration of any plastic deformation or failure during testing, as highlighted by the nearly linear relationship between force and displacement (Figure 3(i)). The microneedles were tested following both printing and coating. At 0.08 N·$Needle^{-1}$ the pristine microneedles recorded a displacement of 48.1 ± 8.79 µm (8.02 ± 1.47%). Following PPy coating, the recorded displacement reduced to 33.7 ± 4.09 µm (5.62 ± 0.68%), indicating an increase in mechanical stiffness following coating. MN-PEDOT:PSS recorded a displacement of 54.7 ± 3.19 µm (9.12 ± 0.53%), an increase from the pristine microneedle displacement, signifying a small reduction in mechanical stiffness following coating. However, no significant difference was observed between the MN-PPy (range 30.4-39.9 µm; $p = 0.06$) and MN-PEDOT:PSS (range 50.5-57.8 µm; $p = 0.51$) apropos to the pristine microneedles (range 38.5-60.2 µm). The recorded displacements are minor compared to the microneedle's initial height of 600 µm, where the nearly linear force-displacement curves denoted the stability of the construct in the tested force range. The mechanical strength of BADGE-PEDOT:PSS microneedles is shown in Figure S9 (Supporting Information).

To assess the skin penetration ability of the microneedles coated with the conductive polymer, ex vivo porcine skin was used as a representative of human skin.[60] Full-thickness porcine skin can be considered a good comparative model to human skin, as it presents a similar composition, with a stratum corneum thickness of 20–26 µm and an epidermis ranging from 30–140 µm compared to 50–120 µm for human skin.[61] The microneedles were subjected to ≈ 5 N (0.5 kg), followed by removal. The resultant pores were imaged using an under light. The MN-PPy achieved 100% skin penetration following the removal of the applied force, as indicated by the corresponding 45 pores imaged (Figure 3(iii)). The MN-PEDOT:PSS achieved 92% penetration success. In both cases, no damage was observed to either the microneedles or surrounding skin following the applied force and skin penetration (Figure 3(iv)). The ex vivo observations, and while considering the total height of the microneedle arrays, could ultimately provide a pain-free minimally invasive platform that has minimal interactions with nerve endings and vascular structures present in the lower dermis. The recorded mechanical properties and successful skin penetration give confidence that the coated microneedles will successfully penetrate the skin in application.

The conductivity and electrochemical performance of the conductive microneedles were evaluated via four-point probe resistivity measurements and cyclic voltammetry (CV). The sheet resistance of the coated microneedles was measured to 8 ± 1 kΩ sq^{-1} at 1 µA for MN-PPy and 324 ± 2 Ω sq^{-1} at 1 µA for MN-PEDOT:PSS (**Table 1**). The MN-PPy resistivity is comparable to recently published work that used platinum-coated polylactic acid microneedles to electropolymerize PPy, with a resistance of 11 kΩ sq^{-1},[62] depicting the ability to attain similar responses without the requirement of a metallic seed layer. The presented sheet resistance for the MN-PEDOT:PSS is optimized toward retaining a thickness that provides sufficient conductivity while maintaining the micromorphology of the microneedles (Table S3, Supporting Information). The resistance values of PEDOT:PSS differ greatly in the literature due to several factors affecting the mechanisms responsible for the conductive nature of the polymer mixture, including the proportion of the two polymers, structural rearrangements, the thickness of the coating, the presence of additives, and the nano/micromorphology of the deposited material.[12,63,64] Nevertheless, similar resistance values to the one obtained in this study have been previously reported in the literature. For instance, a study presented comparable PEDOT:PSS electrical properties when assessed as an electropolymerized thin film for controlling

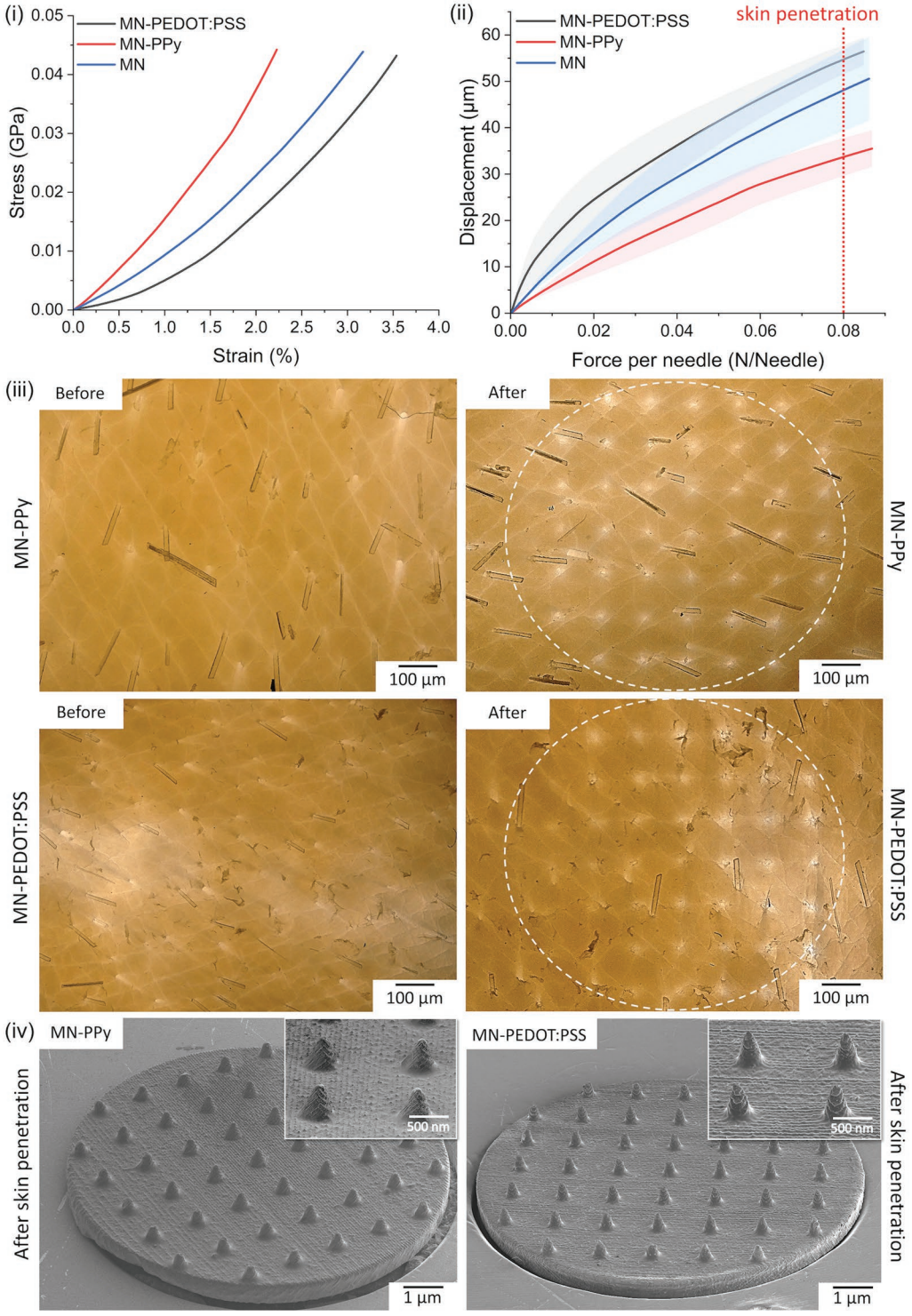

Figure 3. Mechanical testing and ex vivo skin penetration assessment of the microneedle patches. (i) Compression force-displacement curves computed as force per needle. (ii) Nominal stress/strain curves of the microneedle arrays for a maximum applied force of 4 N. (iii) Before and after optical micrographs demonstrating the ability of the microneedle arrays to pierce through the ex vivo skin model when 5 N was applied. (iv) SEM micrographs depicting the retained microneedles' uniformity after skin penetration.

cell growth for tissue engineering, calculated at 360 Ω sq^{-1}.[17] The resistivity values of BADGE-PEDOT:PSS microneedles are shown in Table S4 (Supporting Information).

The CV of MN-PPy and MN-PEDOT:PSS before and after skin penetration (**Figure 4**(i-iv)) was performed to provide mechanistic information regarding the flow of electrons within

Table 1. Resistance values of MN-PEDOT:PSS and MN-PPy at varying currents obtained by measuring the sheet resistance of the coated surfaces using a four-point probe.

MN-PEDOT:PSS	
Current	Resistance
1 µA	$324 \pm 2\ \Omega\ sq^{-1}$
10 nA	$34 \pm 1\ k\Omega\ sq^{-1}$
MN-PPy	
Current	Resistance
1 µA	$8 \pm 1\ k\Omega\ sq^{-1}$
10 nA	$14 \pm 1\ k\Omega\ sq^{-1}$

these composites and to determine changes, if any, in electron transfer subsequent to penetration. Three scan rates, 5, 10, and 20 mV $s^{-1,}$ were cycled over an applied potential range of 1.5 to –1.5 V versus Ag/AgCl. In both instances, all conductive polymer-coated 3D printed microneedle platforms exhibit conductive behavior, where slightly higher currents are observed at faster scan rates.[65] The conducting microneedle surfaces were found to be stable in the range of potential scans of 5–20 mV s^{-1}. Further, a relatively similar shape for all three scan rates was observed, potentially attributed to redox processes within the polymer film.[66] The cycling performance of the microneedle surfaces demonstrates that the coated microneedles are conducting, thus indicating their ability to perform as an electrode. Additionally, the conductive microneedles exhibit stability toward electrochemical modifications in the potential range of the experiment within the supporting phosphate-buffered saline electrolyte (≈ 1 mL droplet). Additionally, the selected electrolyte solution, phosphate buffer, has highlighted its ability to encourage electron transfer at the electrode site, migrating to restore charge equilibrium and complete the electrical circuit.[67]

Two distinctive types of behavior, resulting in unique electrochemical responses, are observed for the two different coatings. For the MN-PPy, oblique and narrow CV voltammograms (Figure 4(i),(iii)) are observed, indicating some form of resistance inside the conducting polymer.[68] For the MN-PEDOT:PSS voltammograms (Figure 4(ii),(iv)), there appears to be visible redox peaks during the scanning procedure due to polymer redox processes inside the conducting polymer.[69]

Interestingly, upon further examination of pre- and post-skin penetration, there appears to be a slight increase within the ranges of current for both coatings. Nevertheless, these alterations do not appear to be significantly different, and thus, skin penetration does not significantly affect the electrical stimulation performance of the fabricated electrodes. To visually demonstrate the 360° electrical conductivity of the microneedle patches, a LED battery indicator circuit was constructed (Figure S10, Supporting Information), where the microneedle arrays were used as a dry electrode (by taping the bottom of the microneedle discs with the wire connected to the anode of 9 V battery) and using the microneedle arrays to switch ON the circuit and light up the LED (Figure 4(v,vi)).

Furthermore, the stability of the PEDOT:PSS and PPy-coated microneedle arrays to withstand multiple skin penetration cycles was evaluated. Although microneedles are conventionally considered single-use patches, it is also of interest to evaluate the coating's performance over multiple penetration cycles for continuous monitoring applications. Coating durability and conductivity were evaluated over five, ten, and twenty penetration cycles into the profile of ex vivo skin (**Figure 5**). Optical micrographs (Figure 5(i)) have demonstrated the ability of both the PEDOT:PSS and PPy-coated microneedle arrays to repeatedly pierce through a skin model, where an approx. force of 5 N (based on the minimum force required for skin penetration[58]) was applied. The stability of coatings was determined through morphological assessment via SEM imaging (Figure 5(ii)), whereas the conductivity performance was determined via cyclic voltammetry following the three skin penetration time points (**Figure 6**). Both PEDOT:PSS and PPy-coated microneedles exhibit retained homogenous microstructural characteristics following all penetration cycles testing, reflective of no observable damage to either the microneedles or surrounding skin following the applied force and skin penetration (Figure 5(ii)). No noteworthy fluctuations were recorded through the cyclic voltammograms collected, depicting negligible variations in the microneedle devices' electrochemical activity following multiple skin penetration cycles (Figure 5(iii)). These observations signify the polymeric coatings' microneedle architecture morphological stability, and electrical durability after multiple applications onto the skin.

To examine the presence of polymer residues upon microneedle insertion, pierced skin specimens and pristine skin were also assessed via FTIR and EDX elemental mapping for the emergence of new peaks and for the quantification of the amounts of the sulfur and nitrogen populations distinctive of the two coatings, respectively. There were no differences observed between the FTIR spectra of the pristine skin grafts and penetrated regions, where the characteristic regions of proteins, lipids, and DNA/RNA were identified (Figure S11, Supporting Information). Additionally, the atomic concentrations from EDX of the pristine and penetrated skin were conceptually similar (Figure S12, Supporting Information), with no significant differences in the atomic concentrations of populations of sulfur and nitrogen being observed (Table S5, Supporting Information). These observations, along with the attained micrographs of the microneedles (Figure 5(ii)), following multiple penetration cycles, indicate the durability of the coatings and the unlikely presence of significant polymer residue upon skin penetration, verifying that the coated layer of both microneedle arrays (PEDOT and PPy) does not peel off during intradermal administration or remove over a sequential period of penetration.

To further validate skin penetration, the ability of the PEDOT:PSS and PPy-coated microneedle arrays to conduct electricity through the skin barrier following penetration was demonstrated. An LED-battery indicator circuit was constructed (Figure S13, Supporting Information). LED glowing can be adjusted by modulating the forward current flow, supplying more current increases light intensity, whereas reducing the current decreases the intensity.[70] The skin is a relatively poor conductor, with the induced current density being the largest near the surface of the skin and exponentially decreasing with increased depth, limiting current flow near the skin's surface

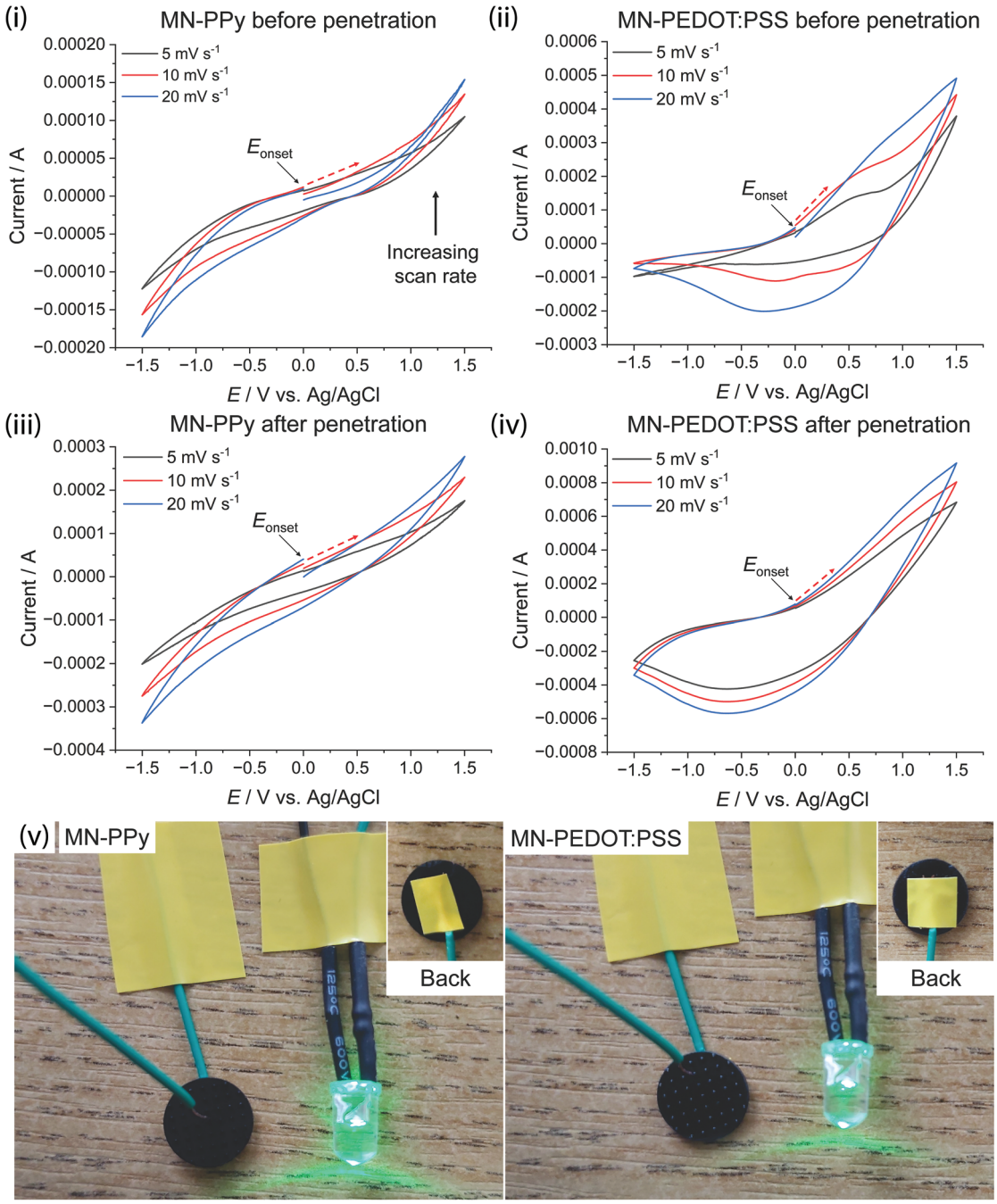

Figure 4. Qualitative analysis of the electrochemical properties of the coated microneedles. (i-iv) Cyclic voltammograms collected in three scan rates: 5, 10, and 20 mV s^{-1} by applying a phosphate-buffered saline droplet (≈ 1 mL) onto the surface of the PPy and PEDOT:PSS microneedle arrays (i-ii) before and (iii-iv) after skin penetration. Recorded in the potential range of 1.5 to -1.5 V (0 V start and stop potential) versus Ag/AgCl (reference electrode), using a Pt wire as the counter electrode. E_{onset}, onset potential. (v-vi) Photographs demonstrating the ability of the (v) MN-PPy and (vi) MN-PEDOT:PSS to act as a dry electrode to light up the LED circuit.

- a phenomenon known as the skin effect.[71] Introducing the highly conductive polymeric microneedle arrays onto the skin can depict effective penetration by increasing the current intensity that flows through the skin layer. Here, an electrode was used to connect the flat bottom side of the microneedle devices to the anode of a 9 V battery, and subsequently applied onto sections of ex vivo dorsal skin. The microneedle-penetrated skin was afterward placed on top of phosphate-buffered saline, where a submerged electrode connected to the cathode of the 9 V battery was used to switch ON the circuit and brightly light up the LED after making contact (Video S1, Figure S13(i, ii), Supporting Information). The MN-PPy and MN-PEDOT:PSS arrays presented a relative brightness of 70% and 101%, respectively. The conductive capabilities of dorsal skin (relative

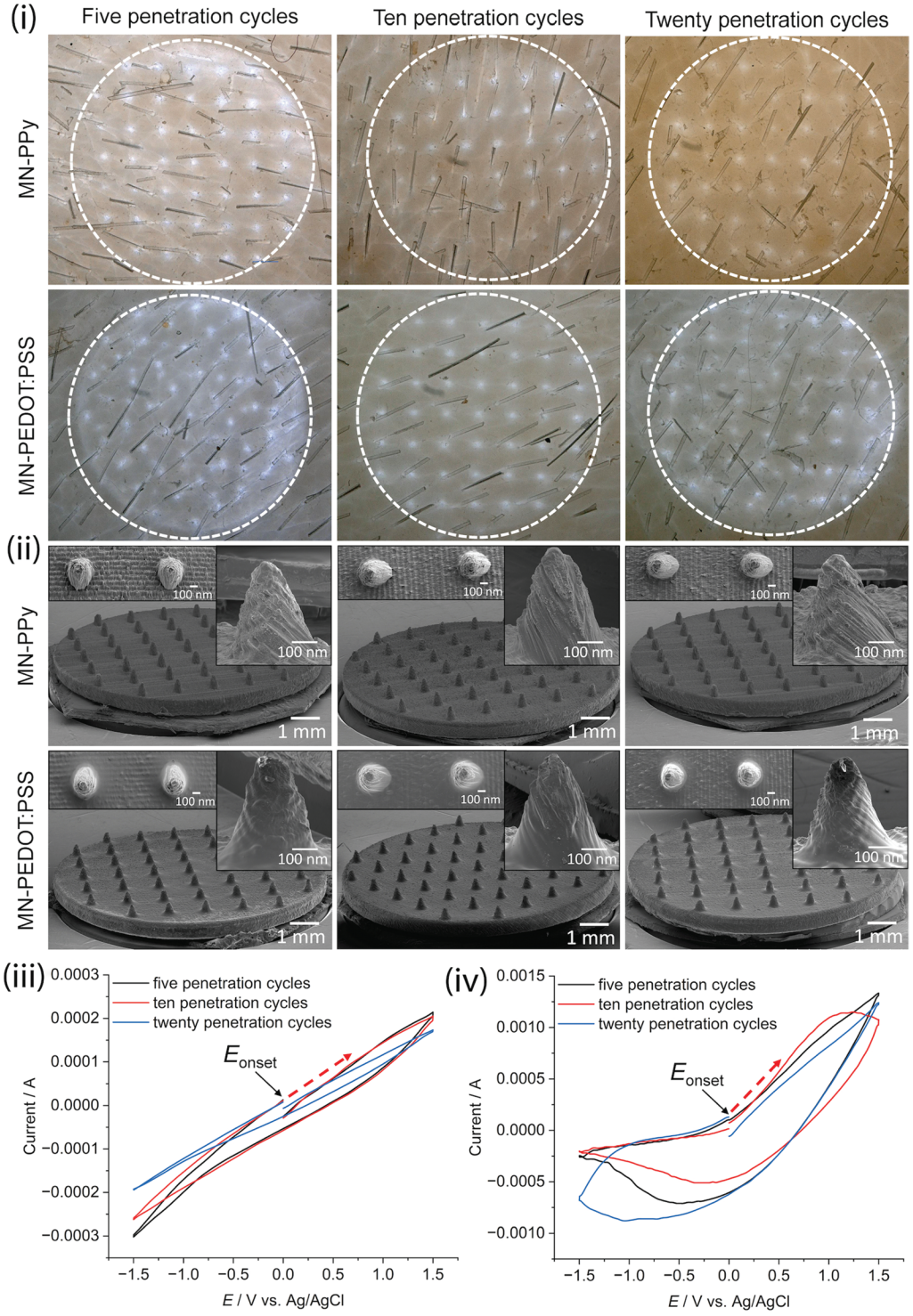

Figure 5. Evaluating the durability of the polymeric conductive microneedle coatings following multiple skin penetration cycles. Ex vivo skin penetration assessment and qualitative analysis of the electrochemical properties of the coated microneedles. (i) Optical micrographs demonstrating the ability of the microneedle arrays to repeatedly pierce through the skin after five, ten, and twenty penetration cycles, where a force of 5 N was applied. (ii) SEM micrographs depicting the retained microneedles' uniformity after the penetration cycles. (iii-iv) Cyclic voltammograms collected at the scan rate of 10 mV s^{-1} by applying a phosphate-buffered saline droplet (≈ 1 mL) onto the surface of the (iii) MN-PPy and (iv) MN-PEDOT:PSS- arrays. Recorded in the potential range of 1.5 to -1.5 V (0 V start and stop potential) versus Ag/AgCl (reference electrode), using a Pt wire as the counter electrode. E_{onset}, onset potential.

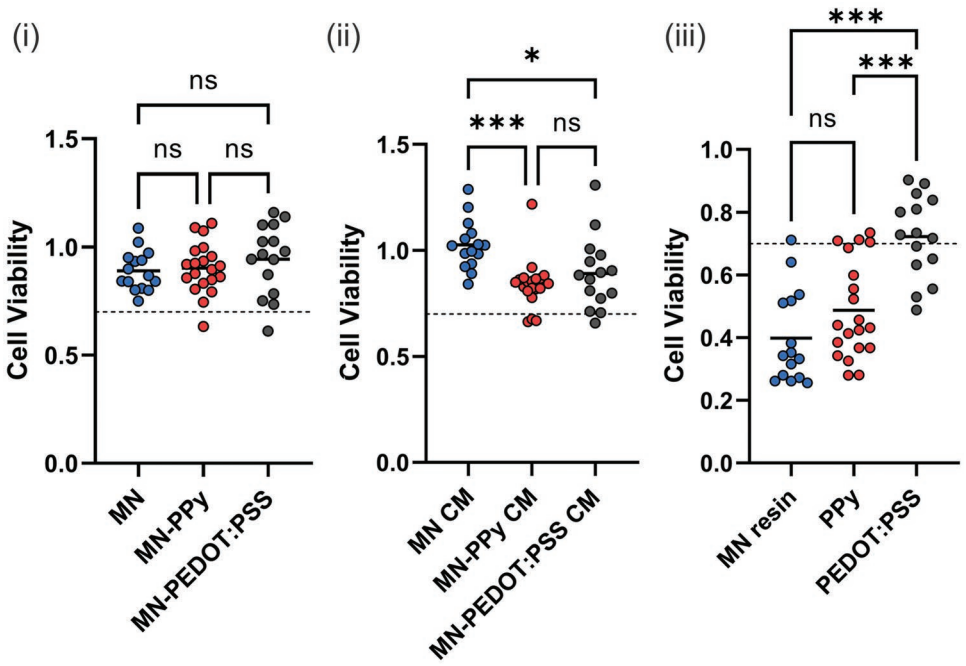

Figure 6. In vitro biocompatibility assessment of the uncoated and coated microneedle devices. Cell viability of HDFs exposed to (i) microneedles devices, (ii) microneedle conditioned media (CM), and (iii) raw material for 24 h. Shown are superplots of N = 3 individual experiments (mean ± SD). Color shades indicate the 5 replicas of each experiment. One-way ANOVA with Tukey's post-hoc test, where n.s.; not significant ($p > 0.05$). The dashed line at 70% depicts the cytotoxic cut off, based on ISO 10993.

brightness 48%) and phosphate-buffered saline (relative brightness 100%) were also demonstrated for comparison (Video S1, Figure S13(iii,iv), Supporting Information). The dorsal skin highlights a low conductivity, and the phosphate-buffered saline shows greater conductivity, as highlighted by the dimly and brightly lit LED light, respectively. Here, the phosphate-buffered saline solution is performing as a *pseudo*-biological medium, demonstrating the devices' ability to effectively conduct through the skin, an essential requirement for the prospective applications of this platform.

In vitro cytotoxicity assays are widely used as endpoint tests when assessing the biocompatibility of medical devices intended for direct or indirect contact with a patient's body.[72] In accordance with ISO 10993, two types of tests, direct contact and extract testing were used in this study. The cell viability of human adult fibroblasts (HDF) was grown in direct contact with the devices for 24 h. Extract testing was used to measure the cytotoxicity of leachable substances from the microneedle devices. To this end, the culture media was incubated with the devices for 24 h at 37 °C prior to exposing the HDF cells to this "leached" culture media (termed "conditioned media" (CM)). According to the ISO standard, a ≥30% reduction of cellular viability after exposure is cytotoxic.

HDF cells in direct contact with pristine microneedles, MN-PPy, and MN-PEDOT:PSS devices had a mean cell viability of 89.1 ± 7.2%, 90.3 ± 6.2%, and 94.4 ± 17.0%, respectively (Figure 6(i)). The presence of the devices resulted in a <30% reduction of cell viability and there were also no significant differences between the devices, demonstrating the non-toxic nature of the conductive layer on the microneedle surface. To further investigate for possible polymer leaching extract testing was conducted. The mean cell viabilities of HDFs exposed to control CM or the CM from the microneedle, MN-PPy and MN-PEDOT:PSS devices were 103.0 ± 9.8%, 84.0 ± 7.6%, and 89.2 ± 14.0%, respectively (Figure 6(ii)). In all instances, the extract from the uncoated and the two different polymer composite-coated microneedle devices did not affect fibroblast viability, demonstrating that no toxic leachable substance from the conductive devices was released during the test period. The stability of the developed constructs' coatings can be further emphasized when compared to the toxicity of the raw materials; microneedle uncured resin, PPy particles, and PEDOT:PSS dispersion, which strongly reduced the HDF viabilities to 40.0 ± 16.5%, 49 ± 13.4%, and 72.3 ± 12.2%, respectively (Figure 6(iii)). Similar results were obtained when BADGE and BADGE-PEDOT:PSS were used (Figure S15 and Table S6, Supporting Information) and the untreated control group data can be found in Figure S16 (Supporting Information). In summary, we did not detect any cytotoxic effect of the two different coatings on fibroblast growth during the 24 h testing period demonstrating a metal-free way of producing biocompatible conductive microneedle surfaces.

3. Conclusion

This work has developed two distinct methodologies for producing novel conductive (metal-free) microneedle platforms by merging 3D printing with conductive polymer coatings. Further, we have provided a versatile approach to producing microneedle arrays based on additive manufacturing using a methacrylic acid-based resin through an easily adaptable CAD

design, with the ability to change the arrays' morphology and architecture. Two of the most well-studied conducting polymers, PPy and PEDOT:PSS, were chosen for this study to illustrate the feasibility of producing polymer-based conductive microneedles as a platform technology and entirely omitting the need for a metallic coating as the interface or seed material for polymer deposition. We have delineated two distinct methodologies based on in situ chemical synthesis (for PPy) and oxygen-plasma surface activation followed by drop casting (for PEDOT:PSS). A morphological, chemical, and physical analysis confirms a homogeneous coating that does not affect the microneedle's microstructure or mechanical properties and an improved water-wetting behavior in comparison to the pristine microneedles. The good conductivity and electrical stability of the polymeric constructs are demonstrated via cyclic voltammetry, resistivity measurements over multiple penetration cycles, and by demonstrating the ability of the microneedle devices to conduct through the skin. Further, we have demonstrated through an in vitro human adult fibroblast study the non-cytotoxic nature of the conductive polymer microneedle devices in comparison to the raw materials, illustrating the stability of the coated surfaces. Finally, the coated microneedles were capable of withstanding the force required for skin penetration and shown to withstand multiple penetration cycles while maintaining conductivity and morphological stability. The presented work ultimately describes two straightforward approaches to developing highly reproducible, low-cost, low-force next-generation microneedle biosensing platforms entirely founded on polymer-based electrode interfaces. The next phase on the road to translation involves incorporating this platform for sensing applications, which can provide a new avenue for developing biosensor platforms for transcutaneous biomarker on-demand monitoring and the construction of wearable smart microneedle patch systems.

4. Experimental Section

Materials: Poly(3,4-ethylenedioxythiophene)-poly(styrenesulfonate) (PEDOT:PSS) 3.0-4.0% in H_2O, high-conductivity grade, was purchased from Sigma-Aldrich (USA). Pyrrole ≥ 98% (PPy) and iron(III) chloride hexahydrate ($FeCl_3{\cdot}6H_2O$) 97% were obtained from Thermo Fisher Scientific (USA). The photocurable stereolithography resin, High Temp Resin (FLHTAM02), was purchased from Formlabs (USA). Polydimethylsiloxane (PDMS), Sylgard™ 184 silicone elastomer kit, was acquired from Dow (USA). Bisphenol A diglycidyl ether resin and diethylenetriamine 99% were purchased from Thermo Fisher Scientific (USA). Ethanol (absolute) 99.8% and acetone 99.5% were obtained from Honeywell (UK). 2-propanol (IPA) ≥ 99.7% was purchased from VWR Chemicals (USA). Deionized water was produced using Purelab® Chorus 1 Complete water purification system (Elga LabWater, Veolia Water Systems LTD).

Dulbecco's Modified Eagle's Medium-high glucose (DMEM) (D6429) and phosphate-buffered saline tablets (P4417) were purchased from Sigma-Aldrich (USA). Foetal bovine serum (FBS) (F9665), penicillin/streptomycin (Merck P4458), and L-glutamine (Merck G7513) were acquired from Merck (Germany). The EZ4U cell proliferation and cytotoxicity assay kit (B1-5000) was obtained from Oxford Biosystems (UK). Copper wire of 99.9% purity and 0.5 mm in thickness (CU510718) was acquired from Advent Research Materials (UK), and the silver-loaded conductive epoxy adhesive (RS-186-3616) was obtained from RS Components (UK). All chemicals were used as received.

Microneedle Design and Fabrication: The computer-aided design (CAD) was developed using AutoCAD (Autodesk, USA). The CAD consisted of a circular base of 10 mm in width and 0.5 mm in thickness, presenting 45 conically shaped needles of 300 µm base diameter and 600 µm height with a 1 mm interneedle spacing. The file was exported as a standard tesselation language (.STL) file and imported into the Preform 3D printing software (FormLabs, USA). The part was first tilted to 45° before generating supports with a reduced touchpoint size and set to print at a 25 µm resolution using the High Temp resin. Following printing, the resultant prints were washed in IPA for 10 min using FormWash and treated at 80 °C under 405 nm UV for 120 min using FormCure. The supports were removed by gently snapping them with a scalpel at the contact point between the supports and the base of the microneedle array.

Chemical Polymerization of PPy onto the Microneedles (MN-PPy): The MN-PPy coating was obtained by in situ chemical oxidative polymerization of the pyrrole monomer using ferric chloride as the oxidizing agent in the presence of the 3D-printed microneedles. The catalyst was prepared by magnetically stirring 2 M pyrrole in ethanol and deionized water (50:50, v/v) for 1 h at room temperature until the solution turned pale yellow. Then, pristine microneedles were added to the solution and magnetically stirred for 3 h at room temperature. The microneedles were subsequently transferred to a 0.25 M aqueous solution of $FeCl_3{\cdot}6H_2O$ at 5 °C. The microneedles were allowed to polymerize at room temperature for 24 h while undergoing magnetic stirring, producing a black-colored product. The resultant product formulated an all-around polypyrrole layer onto the surface of the microneedles. To ensure a homogenous coating, the microneedles were subjected to sequential washes: magnetically stirred in ethanol and deionized water for 1 h, sonicated in deionized water for 30 min, washed in deionized water, and left overnight while magnetically stirred in deionized water. The final product was air-dried to remove the excess water and vacuum dried for 4 h at 50 °C.

Microneedle-PEDOT:PSS Coating (MN-PEDOT:PSS): High-temperature resin microneedles were oxygen plasma treated using a Zepto Model 2 Diener Plasma Reactor (Diener Electronics, Germany) at a plasma power of 100 W, exposure time of 10 min, and an oxygen flow rate of 1 mbar. Within 10 min of post-plasma treatment, 25 µL of PEDOT:PSS was pipetted onto one side of the treated microneedles and dried in a fan oven at 60 °C for 20 min. Coated microneedles were removed from the oven and flipped over, where this process was repeated on the bare flat side. The entirety of this protocol was repeated to achieve a total of two even coatings on each side.

Chemical and Physical Characterization: FTIR: Each Fourier-transform infrared spectroscopy (FTIR) spectrum represents the average of 126 scans in the wavenumber range of 4500–500 cm^{-1} with a spectral resolution of 1 cm^{-1}, obtained through the iD7 attenuated total reflectance (ATR)-mode of a Nicolet™ iS5 FTIR spectrometer (Thermo Fisher Scientific, USA).

Raman: Raman spectra were collected using an inVia™ confocal Raman microscope (Renishaw, UK). The specimens were irradiated using a green line laser (wavelength 532 nm) set at 5% (69 mW) power, where 10 s exposure with three accumulations point spectra were obtained under ambient conditions.

Water Sessile Drop Evaluation: The surface chemistry of flat uncoated and coated surfaces was investigated using a contact angle measurement system, OCA 25 (Data Physics, UK), at ambient temperature (21 °C). A 5 µL deionized water droplet was dispensed at the surface of each vacuum-dried specimen and allowed to settle for 30 s, where a photograph was taken and analyzed using Fiji-ImageJ, contact angle add-on, (v.1.8, National Institutes of Health, USA). The surface energy was evaluated as the adhesion energy between the flat coated and uncoated surfaces, and the surface tension of deionized water at 21 °C as per the Young-Dupre equation (Equation 1), where W_{sl} the energy of adhesion, σ_l the surface tension of the liquid and θ the contact angle.

$$W_{sl} = \sigma_l(1+\cos\theta) \quad (1)$$

Morphological Assessment and Surface Chemistry: SEM imaging: The surface morphology was assessed using a SU3900 scanning electron

microscopy (SEM) instrument (Hitachi, Japan). Before analysis, the samples were mounted onto aluminum stubs using carbon tape and evacuated overnight. The samples were then coated with a 10 nm thin layer of gold using a Q150TS Plus sputter coater (Quorum, USA). High-resolution micrographs were captured from a 10 to 70 mm working distance at an operating accelerating voltage of 5–15 kV, at tilt angles from 0° to 70°. The chemical composition of the surfaces was carried out via elemental mapping by energy-dispersive X-ray (EDX) spectroscopy using a 170 mm^2 Ultim Max EDX detector (Oxford Instruments, UK) attached to the SEM. The data were interpreted using the AZtec software package.

AFM imaging: To assess the surface roughness of the various microneedles, the Jupiter XR (Oxford Instruments) atomic force microscope (AFM) was used in blueDrive™ Tapping Mode with AC160TS-R3 tips. Sample microneedles were flipped, and the undersides were imaged in 10×10 µm sections in 10 different areas per sample to obtain representative images and roughness. Height and amplitude traces were extracted, and an analysis of root mean square (RMS) surface roughness was performed on Gwyddion using the statistical quantities tool.

Macroscopic imaging: Macroscopic images of the microneedles were attained using a 10X-200X USB digital microscope with a 0.3-megapixel resolution (United Scope, Netherlands).

Resistance, Electrochemical Evaluation, and Battery-LED System: Four-point probe measurements: The resistivity of flat-coated surfaces was evaluated by measuring the sheet resistance using a four-point probe: Jandel RM3000 (Jandel Engineering, UK). The RM3000 presents four equally spaced contacts, with probe spacing of ~ 1 mm, and can obtain readings ranging from 1 mOhm sq^{-1} to 5×10^8 Ohm sq^{-1} at a 0.5% accuracy. This equipment comprises a probe station (four probe tips), an ampere meter, a DC current source, and a voltmeter. Current flowed between the outer probes, allowing for the decreasing voltage across the inner probes to be measured. For the measurement procedure, MN-PEDOT:PSS and MN-PPy samples were individually aligned directly beneath the probe head on the anodized aluminum base. The voltage was allowed to stabilize, and resistivity measurements were recorded. After each completed measurement, samples were removed and replaced with fresh ones. A total of three measurements were recorded for each batch of MN-PPy and MN-PEDOT:PSS samples (BADGE-PEDOT:PSS resistance measurements are reported in Table S5, Supporting Information). The reported error on the average was evaluated as the standard deviation of the collection of each individual group's measurements as performed for each material. The sheet resistance (*Rs*) was calculated as shown in Equation 2 below, where *k* the geometric factor for thin coatings (≈4.53), *V* the voltage, and *I* the current.

$$Rs = k\frac{V}{I} \tag{2}$$

Cyclic voltammetry: For electrical measurements, the bottom of the coated microneedle discs was connected to a copper wire using silver-loaded conductive epoxy (thermal conductivity 11 W mK^{-1}). The silver epoxy was cured at 60 °C for 2 h to obtain the required electrical connection and mechanical stability. The electrochemical experiments were performed on a µAutolab type II potentiostat/galvanostat (Metrohm, Switzerland) in the cyclic voltammetry (CV) potentiostatic three-electrode configuration, controlled by the Nova v.2.1 software. Cyclic voltammograms were collected in three scan rates: 5, 10, and 20 $mV{\cdot}s^{-1}$ by applying a phosphate-buffered saline droplet onto the surface of the microneedle arrays, recorded in the potential range of 1.5 to –1.5 V (0 V start and stop potential) versus an Ag/AgCl electrode, using a Pt wire (purity 99.95% and thickness 0.5 mm) as the counter electrode. All the measurements were obtained in a Faraday cage at room temperature.

Battery-LED visual depiction and conductivity following skin penetration: To visually demonstrate the ability of the conducting microneedle layer to glow a light-emitting diode (LED), a simple LED-battery (9 V) circuit was designed. The battery's anode was taped to stay in contact with the base of the microneedles and the short lead of the LED, whereas the cathode's wire was used as a switch that turned it on when in contact with the individual microneedle tips.

The capability of the microneedle devices to conduct through the skin barrier after microneedle penetration was further evaluated. A Petri dish was filled with PBS pH 7.2, where an electrode connected to the cathode of a 9 V battery through a LED was submerged into the pool. A circular opening was made in the Petri dish's lid. The electrode (anode) was connected to the microneedle device's base, and thumb pressure was applied to a section of porcine skin to penetrate it. This was subsequently placed on top of the Petri dish's lid opening. This formed a close circuit via the current traveling through the skin barrier onto the PBS, lightening the LED. As a control, skin-only and PBS-only were also assessed. Based on Mean Gray Value (MGV) and integrated density, light intensity was computed using Fiji-ImageJ software (v.1.8, National Institutes of Health, USA). From this, the relative brightness (*RB*, %) was calculated using equation 3. The setup is depicted in Figure S14 (Supporting Information).

$$RB(\%) = \frac{MGV_{Group}}{MGV_{PBS\ only}} \times 100 \tag{3}$$

Mechanical Characterization and Microneedles Penetration Study: Dynamic Mechanical Analyser: The mechanical properties of the conductive microneedles were evaluated using the Mettler Toledo DMA1 (Mettler Toledo, USA) dynamic mechanical analyser (DMA). The microneedles were attached to a bottom titanium plate, while the upper titanium plate was lowered until contact was made with the microneedle tips, indicated by a recorded force on the equipment screen. A compressive force from the bottom plate was applied from 0 to 4 N at a rate of 0.25 $N{\cdot}min^{-1}$, with the resultant displacement recorded. The samples were imaged following testing to monitor the effect of the compression on the microneedles.

Ex vivo skin penetration: Excised porcine skin was obtained from a local abattoir. Normal high-temperature cleaning procedures were not used to preserve the integrity of the skin barrier. Within 24 h of slaughter, the porcine skin was washed with water, sliced with a dermatome to a nominal thickness of 750 µm, and frozen. Before use, the frozen skin was thawed and cut down to ~ 2 $cm^{2,}$ and placed on a supporting structure. The MN-PPy and MN-PEDOT:PSS were placed on top of the skin, and 500-gram mass was applied (equating to ≈ 5 N). This was maintained for 60 s prior to removal, and the resultant pores were analyzed using optical microscopy. The %Penetration was calculated by assessing the number of needles penetrated (N_P) against the total number of needles (N_T) (Equation 4).

$$\%Penetration = \frac{N_P}{N_T} \times 100 \tag{4}$$

Evaluating the microneedles coating's durability to withstand multiple penetration cycles: The MN-PPy and MN-PEDOT:PSS were placed on top of the dorsal section of skin where a 500-gram weight was applied for 10 s; following removal, the weight was reapplied for a total of five, ten, or twenty sequential applications. Successful penetration was evaluated via light microscopy. The stability of the coating was determined via SEM microscopy. The presence of residual polymer in the penetrated skin was examined via EDX and FTIR, following precisely the same parameters as aforementioned.

In Vitro Biocompatibility Assessment of the Microneedle-Coatings: Cell culture: Adult human dermal fibroblasts (HDF) were generously provided by the Walko lab, from stocks originally obtained from the Watt laboratory.[73] Cells were routinely subject to mycoplasma testing. All cells were cultured at 37 °C and 5% CO_2 and were passaged when ~ 80% confluent. HDFs were cultured in DMEM supplemented with 10% foetal bovine serum (Merck F9665), 1% Penicillin/Streptomycin (Merck P4458), and 2 mM L-glutamine (Merck G7513).

Viability assay: For viability assays, 2×10^4 cells/well were seeded into 24-well plates. After 24 h, cells were exposed to one microneedle array per well, conditioned media, or control conditions (see treatment conditions). 24-h post-treatment, cell viability was measured using

the EZ4U cell proliferation and cytotoxicity assay kit according to the manufacturer's instructions (Oxford BioSystems B1-5000). In brief, 100 µL of 1:10 diluted EZ4U substrate was added per well and incubated at 37 °C for 1.5 h. The supernatant was transferred to a flat bottom 96-well plate to measure the absorbance at 450 nm using a BMG FLUOstar Omega (BMG Labtech, UK) plate reader. Viability values were normalized to the viability of untreated cells, grown in tissue culture Petri dishes, which served as a negative control, as shown in Figure S16 (Supporting Information).

Treatment conditions: For direct contact assays, sterilized microneedle arrays with 20 mm^2 surface area were added directly to the cultured cells. To test the effects of leachable substances from the microneedle arrays, the cell culture medium was incubated with the devices for 24 h at 0.5 mL per 20 mm^2 microneedle array at 37 °C before being added to the cells. As a positive control for cytotoxic effects, the uncured resin was incubated with cell culture media (1/4 v/v) for 24 h and then added to cells.

Supporting Information

Supporting Information is available from the Wiley Online Library or from the author.

Acknowledgements

A.K., Y.L.M., and J.G.T. contributed equally to this work. This research was financially supported by the Engineering and Physical Sciences Research Council Grant EP/V010859/1 and the Royal Society Research Grant RSG\R1\201185. The authors would like to thank Lina Wang and Victor Li for their assistance with the CV and sample preparation inductions. The authors recognize the Material and Chemical Characterisation Facility (MC^2) at the University of Bath (doi.org/10.15125/mx6j-3r54) and Dr. Philip Fletcher's electron microscopy expertise and assistance. Last, the authors would like to thank the Department of Chemistry at the University of Bath for allowing us to use some of the analytical equipment in their facilities. The authors thank Professor Richard Guy for his expertise and donation of porcine skin during experimentation. The authors acknowledge the Micro-Mechanical Facility, in the Faculty of Engineering, University of Bath. The authors thank the editor and reviewers for their constructive comments which improved the manuscript.

Conflict of Interest

The authors declare no conflict of interest.

Data Availability Statement

The data that support the findings of this study are openly available in Dataset for Conductive polymer-coated 3D printed microneedles: biocompatible platforms for minimally invasive biosensing interfaces at https://doi.org/10.15125/BATH-01210, reference number 1210.

Keywords

biocompatible, biosensors, conductive microneedles, PEDOT:PSS, polypyrrole, stereolithography 3D printing

Received: October 13, 2022
Revised: December 13, 2022
Published online: January 3, 2023

[1] P. Li, G.-H. Lee, S. Y. Kim, S. Y. Kwon, H.-R. Kim, S. Park, *ACS Nano* **2021**, *15*, 1960.
[2] J. Kim, A. S. Campbell, B. E.-F. de ĀVila, J. Wang, *Nat. Biotechnol.* **2019**, *37*, 389.
[3] M. A. Ali, C. Hu, E. A. Yttri, R. Panat, *Adv. Funct. Mater.* **2022**, *32*, 2107671.
[4] J. G. Turner, L. R. White, P. Estrela, H. S. Leese, *Macromol. Biosci.* **2021**, *21*, 2000307.
[5] A. A. Hamzah, S. Nadzirah, B. Development, in *Reference Module in Biomedical Sciences*, Elsevier, Raleigh, USA **2022**.
[6] P. P. Samant, M. M. Niedzwiecki, N. Raviele, V. Tran, J. Mena-Lapaix, D. I. Walker, E. I. Felner, D. P. Jones, G. W. Miller, M. R. Prausnitz, *Sci. Transl. Med.* **2020**, *12*, 571.
[7] S. R. Dabbagh, M. R. Sarabi, R. Rahbarghazi, E. Sokullu, A. K. Yetisen, S. Tasoglu, *iScience* **2021**, *24*, 102012.
[8] O. Erdem, I. Es, G. A. Akceoglu, Y. Saylan, F. Inci, *Biosensors* **2021**, *11*, 296.
[9] J. Madden, C. O'Mahony, M. Thompson, A. O'Riordan, P. Galvin, *Sens. Biosensing Res.* **2020**, *29*, 100348.
[10] H. Lu, S. Zada, L. Yang, H. Dong, *Front. Bioeng. Biotechnol.* **2022**, *10*, 851134.
[11] T. M. Rawson, S. A. N. Gowers, D. M. E. Freeman, R. C. Wilson, S. Sharma, M. Gilchrist, A. Macgowan, A. Lovering, M. Bayliss, M. Kyriakides, P. Georgiou, A. E. G. Cass, D. O'Hare, A. H. Holmes, *Lancet Digit Health* **2019**, *1*, e335.
[12] X. Fan, W. Nie, H. Tsai, N. Wang, H. Huang, Y. Cheng, R. Wen, L. Ma, F. Yan, Y. Xia, *Adv. Sci.* **2019**, *6*, 1900813.
[13] Y. Liang, J. C.-H. Goh, *Bioelectricity* **2020**, *2*, 101.
[14] G. Kaur, R. Adhikari, P. Cass, M. Bown, P. Gunatillake, *RSC Adv.* **2015**, *5*, 37553.
[15] H. He, L. Zhang, X. Guan, H. Cheng, X. Liu, S. Yu, J. Wei, J. Ouyang, *ACS Appl. Mater. Interfaces* **2019**, *11*, 26185.
[16] S. Kim, W.-K. Oh, Y. S. Jeong, J.-Y. Hong, B.-R. Cho, J.-S. Hahn, J. Jang, *Biomaterials* **2011**, *32*, 2342.
[17] M. Marzocchi, I. Gualandi, M. Calienni, I. Zironi, E. Scavetta, G. Castellani, B. Fraboni, *ACS Appl. Mater. Interfaces* **2015**, *7*, 17993.
[18] N. K. Rawat, R. Ghosh, in *Nanosensors for Smart Cities*, (Eds.: B. Han, V. K. Tomer, T. A. Nguyen, A. Farmani, P. K. Singh), Elsevier, San Diego, USA **2020** pp. 129–142.
[19] J. Ouyang, *SmartMat* **2021**, *2*, 263.
[20] C. Xu, D. Jiang, Y. Ge, L. Huang, Y. Xiao, X. Ren, X. Liu, Q. Zhang, Y. Wang, *Chem. Eng. J.* **2022**, *431*, 134109.
[21] A. T. Mai, T. P. Duc, X. C. Thi, M. H. Nguyen, H. H. Nguyen, *Appl. Surf. Sci.* **2014**, *309*, 285.
[22] W. Hai, T. Goda, H. Takeuchi, S. Yamaoka, Y. Horiguchi, A. Matsumoto, Y. Miyahara, *Sens. Actuators, B* **2018**, *260*, 635.
[23] Y. Liang, A. Offenhāusser, S. Ingebrandt, D. Mayer, *Adv. Healthcare Mater.* **2021**, *10*, 2100061.
[24] M. Bansal, A. Dravid, Z. Aqrawe, J. Montgomery, Z. Wu, D. Svirskis, *J. Controlled Release* **2020**, *328*, 192.
[25] B. L. Zhang, Y. Yang, Z. Q. Zhao, X. D. Guo, *Electrochim. Acta* **2020**, *358*, 136917.
[26] U. Heredia Rivera, S. Kadian, S. Nejati, J. White, S. Sedaghat, Z. Mutlu, R. Rahimi, *ACS Sens.* **2022**, *7*, 960.
[27] K. J. Lee, S. S. Jeong, D. H. Roh, D. Y. Kim, H.-K. Choi, E. H. Lee, *Int. J. Pharm.* **2020**, *573*, 118778.
[28] K. O'Brien, A. Bhatia, F. Tsen, M. Chen, A. K. Wong, D. T. Woodley, W. Li, *PLoS One* **2014**, *9*, e113956.
[29] K. J. Krieger, N. Bertollo, M. Dangol, J. T. Sheridan, M. M. Lowery, E. D. O'Cearbhaill, *Microsyst. Nanoeng.* **2019**, *5*, 42.
[30] S. N. Economidou, D. Douroumis, *Adv. Drug Delivery Rev.* **2021**, *173*, 60.
[31] L. Fang, H. Ren, X. Mao, S. Zhang, Y. Cai, S. Xu, Y. Zhang, L. Li, X. Ye, B. Liang, *Biosensors* **2022**, *12*, 102.

[32] S. A. N. Gowers, D. M. E. Freeman, T. M. Rawson, M. L. Rogers, R. C. Wilson, A. H. Holmes, A. E. Cass, D. O'Hare, *ACS Sens.* **2019**, *4*, 1072.
[33] S. Miao, H. Cui, T. Esworthy, B. Mahadik, S.-j. Lee, X. Zhou, S. Y. Hann, J. P. Fisher, L. G. Zhang, *Adv. Sci.* **2020**, *7*, 1902403.
[34] Y. Wang, et al., *ACS Appl. Mater. Interfaces* **2021**, *13*, 12746.
[35] Y. Yin, M. Prabhakar, P. Ebbinghaus, C. Correa Da Silva, M. Rohwerder, *Chem. Eng. J.* **2022**, *440*, 135739.
[36] M. Liu, X. Yang, W. Shao, T. Wu, R. Ji, B. Fan, G. Tong, *Carbon* **2021**, *174*, 625.
[37] F. Imani, R. Karimi-Soflou, I. Shabani, A. Karkhaneh, *Polymer* **2021**, *218*, 123487.
[38] L. Zhang, Y. Wu, Y. Xia, L. Jin, *Electrochim. Acta* **2022**, *412*, 140108.
[39] S. Akerboom, et al., *ACS Appl. Mater. Interfaces* **2015**, *7*, 16507.
[40] X. Huang, Y.-H. Yu, O. L. de Llergo, S. M. Marquez, Z. Cheng, *RSC Adv.* **2017**, *7*, 9495.
[41] J. J. Lee, S. Gandla, B. Lim, S. Kang, S. Kim, S. Lee, S. Kim, *NPG Asia Mater.* **2020**, *12*, 65.
[42] C. Duc, A. Vlandas, G. G. Malliaras, V. Senez, *Soft Matter* **2016**, *12*, 5146.
[43] B. Baruah, A. Kumar, *Electroanalysis* **2018**, *30*, 2131.
[44] A. C. Bhowal, H. Talukdar, S. Kundu, *Polym. Bull.* **2018**, *76*, 5233.
[45] P. S. Devi, S. N. Chanu, P. Dasgupta, B. S. Swain, B. P. Swain, *Appl. Phys. A* **2022**, *128*, 403.
[46] S. V. Selvaganesh, J. Mathiyarasu, K. L. N. Phani, V. Yegnaraman, *Nanoscale Res. Lett.* **2007**, *2*, 546.
[47] A. B. Horn, K. Jessica Sully, *Phys. Chem. Chem. Phys.* **1999**, *1*, 3801.
[48] S. Sain, D. Ray, A. Mukhopadhyay, S. Sengupta, T. Kar, C. J. Ennis, P. K. S. M. Rahman, *J. Appl. Polym. Sci.* **2012**, *126*, E127.
[49] A. Barkane, O. Platnieks, M. Jurinovs, S. Gaidukovs, *Polym. Degrad. Stab.* **2020**, *181*, 109347.
[50] S. A. Brinckmann, N. Patra, J. Yao, T. H. Ware, C. P. Frick, R. S. Fertig, *Adv. Eng. Mater.* **2018**, *20*, 1800593.
[51] E. Marin, F. Boschetto, M. Zanocco, H. N. Doan, T. P. M. Sunthar, K. Kinashi, D. Iba, W. Zhu, G. Pezzotti, *Polym. Degrad. Stab.* **2021**, *185*, 109503.
[52] R. Al-Kasasbeh, A. J. Brady, A. J. Courtenay, E. Larraneta, M. T. C. McCrudden, D. O'Kane, S. Liggett, R. F. Donnelly, *Drug Delivery Transl. Res.* **2020**, *10*, 690.
[53] V. Sharma, D. S. Patel, V. K. Jain, J. Ramkumar, *Int. J. Mach. Tools Manuf.* **2020**, *155*, 103579.
[54] Z. Niu, E. Zheng, H. Dong, G. A. Tosado, Q. Yu, *ACS Appl. Energy Mater.* **2020**, *3*, 9656.
[55] T. W. Bacha, D. C. Manuguerra, R. A. Marano, J. F. Stanzione, *RSC Adv.* **2021**, *11*, 21745.
[56] C. Tzivelekis, M. P. Selby, A. Batet, H. Madadi, K. Dalgarno, *J. Micromech. Microeng.* **2021**, *31*, 035005.
[57] A. Patel, O. Kravchenko, I. Manas-Zloczower, *Polymers* **2018**, *10*, 125.
[58] S. P. Davis, B. J. Landis, Z. H. Adams, M. G. Allen, M. R. Prausnitz, *J. Biomech.* **2004**, *37*, 1155.
[59] M. A. Lopezâ Ramirez, F. Soto, C. Wang, R. Rueda, S. Shukla, C. Silva-Lopez, D. Kupor, D. A. McBride, J. K. Pokorski, A. Nourhani, N. F. Steinmetz, N. J. Shah, J. Wang, *Adv. Mater.* **2020**, *32*, 1905740.
[60] A. Summerfield, F. O. Meurens, M. E. Ricklin, *Mol. Immunol.* **2015**, *66*, 14.
[61] L. K. Branski, R. Mittermayr, D. N. Herndon, W. B. Norbury, O. E. Masters, M. Hofmann, D. L. Traber, H. Redl, M. G. Jeschke, *Burns* **2008**, *34*, 1119.
[62] Y. Yang, et al., *ACS Appl. Mater. Interfaces* **2022**, *14*, 31645.
[63] N.'A. Shahrim, Z. Ahmad, A. Wong Azman, Y. Fachmi Buys, N. Sarifuddin, *Materials Advances* **2021**, *2*, 7118.
[64] S. Zhang, P. Kumar, A. S. Nouas, L. Fontaine, H. Tang, F. Cicoira, *APL Mater.* **2014**, *3*, 014911.
[65] J. - M. Savéant, C. Costentin, in *Elements of Molecular and Biomolecular Electrochemistry*, (Eds.: J.-M. Savéant, C. Costentin), John Wiley & Sons, Hoboken , NJ **2019**, p. 1–80.
[66] D. Zhao, Q. Zhang, W. Chen, X. Yi, S. Liu, Q. Wang, Y. Liu, J. Li, X. Li, H. Yu, *ACS Appl. Mater. Interfaces* **2017**, *9*, 13213.
[67] N. Elgrishi, K. J. Rountree, B. D. Mccarthy, E. S. Rountree, T. T. Eisenhart, J. L. Dempsey, *J. Chem. Educ.* **2018**, *95*, 197.
[68] P. Si, S. Ding, X.-W. (.D.) Lou, D.-H. Kim, *RSC Adv.* **2011**, *1*, 1271.
[69] Y. S. Choudhary, L. Jothi, G. Nageswaran, in *Spectroscopic Methods for Nanomaterials Characterization*, (Eds.: S. Thomas), Elsevier, Amsterdam **2017**, pp. 19–54.
[70] G. Held, *Introduction to Light Emitting Diode Technology and Applications*, 1 ed., Auerbach Publications, New York **2008**, p. 192.
[71] A. Todoroki, *Adv. Compos. Mater.* **2012**, *21*, 477.
[72] ISO 10993–5:2009: Biological evaluation of medical devices — Part 5: Tests for in vitro cytotoxicity, T.C.I.T. 194, Editor. 2009, International Organization for Standardization. p. 34.
[73] G. Walko, S. Woodhouse, A. O. Pisco, E. Rognoni, K. Liakath-Ali, B. M. Lichtenberger, A. Mishra, S. B. Telerman, P. Viswanathan, M. Logtenberg, L. M. Renz, G. Donati, S. R. Quist, F. M. Watt, *Nat. Commun.* **2017**, *8*, 14744.